

EXPERIMENTAL AND NUMERICAL INVESTIGATION ON SEPARATION CHARACTERISTICS OF SERPENTINE CONVERGENT-DIVERGENT NOZZLE

Mingxin Wang¹, Li Zhou^{1,2}, Jingwei Shi¹, Wenjian Deng¹, Hong Xiao¹

School of Power and Energy, Northwestern Polytechnical University, Xi'an 710072, China
Collaborative Innovation Center for Advanced Aero-Engine, Beijing 100191, China

Abstract

The serpentine convergent-divergent nozzle combines the high stealth and wide speed range characteristics required by future warplanes. However, it faces the same problems of flow separation and lateral load under over-expanded state as the axisymmetric convergent-divergent nozzle. Due to the special curved configuration and round-to-square cross-section design of the serpentine nozzle, there are complex pressure gradients and strong swirling flow characteristics inside the nozzle affecting the flow separation characteristics under over-expanded state. This paper constructs a design Mach number 2 serpentine convergent-divergent nozzle model, and carries out experimental and numerical investigation on the serpentine convergent-divergent nozzle with a nozzle pressure ratio(NPR) ranging from 1.4 to 3.0, with a view to obtaining the flow separation mechanism. The flow separation characteristics of the serpentine convergent-divergent nozzle were obtained experimentally using a schlieren system, PSI electronic pressure scanning valves and a six-component balance system. The internal flow within the serpentine convergent section is complex, causing the jet at the entrance of the divergent section to exhibit a vertically asymmetric and laterally non-uniform distribution. This leads to the jet in the divergent section deflecting upwards at low NPRs, and there are differences in the flow separation structures in different vertical planes within the divergent section. When a double "λ" shock structure appears, layered flow is observed. As the NPR increases, the flow separation structure transitions from an asymmetric upper restricted shock separation(RSS)-lower free shock separation(FSS) to an asymmetric FSS-FSS structure, and finally to a symmetric FSS-FSS structure, with the jet deflection disappearing. The separation shock within the nozzle exhibits a threedimensional pattern, with double " λ " shock structures present in both vertical and horizontal planes. As the NPR increases, the thrust vector angle first increases and then decreases, while the axial thrust coefficient exhibits the opposite trend.

Keywords: serpentine convergent-divergent nozzle; experimental and numerical investigation; flow separation mechanism; nozzle pressure ratio; separation structure.

1. Introduction

With the deepening of information technology in modern warfare, high stealth and wide-speed range have become the key features of air superiority fighters[1-3]. Serpentine nozzles, with their serpentine curved surfaces, can obstruct the propagation of infrared signals from high-temperature components[4]. Additionally, they reflect and dissipate electromagnetic waves entering the nozzle, significantly reducing the infrared radiation and electromagnetic scattering characteristics of aircraft engines[5]. This greatly enhances the rearward stealth capabilities of aircraft and has been practically applied in various fighter jets, including the U.S. B-2 bomber, Sweden's "Eikon" UAV, France's "Neuron" UAV, and the UK's "Taranis" UAV[6-9]. However, conventional serpentine convergent nozzles are insufficient to meet the wide speed range characteristics of fighter jets. Consequently, serpentine convergent-divergent nozzles have emerged as the inevitable exhaust system

configuration to meet these stringent demands. Nonetheless, they face the same issues as conventional convergent-divergent nozzles under over-expanded state. When the NPR is lower than the design NPR, severe shock/boundary layer interaction problems can occur within the nozzle, leading to unintended thrust deviation, flow separation, and lateral loads[10, 11]. These issues can damage the nozzle structure and increase the difficulty of controlling the aircraft.

In the past, many researchers have conducted experimental and numerical studies to investigate the flow characteristics of nozzles under over-expanded state at different NPRs. Reijasse et al. [12, 13] studied the unsteady nature of symmetric and asymmetric shocks in a supersonic dual-throat planar nozzle in the Onera S8Ch wind tunnel. The study showed that the wall roughness upstream of the shock can induce shock asymmetry, while the geometric asymmetry of the second throat does not affect the shock asymmetry. The formation of symmetric or asymmetric shock structures depends on the throat contraction ratio of the wind tunnel (second throat height/first throat height).

Johnson and Papamoschou et al. [14, 15] conducted experimental studies on flow separation in planar convergent-divergent nozzles within the range of nozzle exit-to-throat area ratios A_e/A_t =1.0 to 1.5 and the NPR=1.2 to 1.8. Their research indicated that when A_e/A_t >1.4, asymmetric separation occurs in the nozzle, where one foot of the lambda shock is larger than the other, and this asymmetry does not change during a single experiment but may change during a restart. For larger NPR and A_e/A_t , the shocks are unsteady. The separation shear layer of the large lambda shock angle exhibits strong instability, forming large vortices downstream of the nozzle exit, which is key to enhancing mixing. They suggested that a potential source of jet instability is the interaction between unsteady waves generated by the main separation shock and the shear layer of the large separation region. Xiao et al. [16, 17]conducted a numerical study using the k- ω turbulence model to investigate the flow separation in the nozzles used in Papamoschou's experiments, within the nozzle exit-to-throat area ratio A_e/A_t =1.0 to 1.8 and the NPR=1.2 to 1.8. The study showed that the k- ω SST turbulence model best captures the experimental shock locations and pressure distribution. When 1.5 < NPR < 2.4, different initial flow fields may cause symmetric and asymmetric separations.

Hunter et al. [18, 19]conducted experimental and two-dimensional numerical simulation studies on a non-axisymmetric, two-dimensional convergent-divergent nozzle with a design NPR of 8.8 and an exit Mach number of 2.1 in NASA Langley's 16-foot transonic wind tunnel. The research showed that, under over-expanded state, the flow was predominantly characterized by shock-induced boundary layer separation, which manifested in two distinct flow patterns: for NPR<1.8, there was threedimensional separation with partial reattachment, and for NPR>2.0, there was two-dimensional complete separation. As the nozzle transitioned from one state to another, a significant transformation was observed. They also noted asymmetric separation during the experiments, which they did not attribute to the sensitivity of the starting conditions but rather to the natural tendency of the overexpanded nozzle flow separation to achieve more effective thermodynamic equilibrium. Building on Hunter's experimental results, Hamed et al.[20, 21] performed two-dimensional numerical simulations of the over-expanded nozzle flow using different turbulence models. They found that the two-equation turbulence models better predict shock locations, among which the Wilcox k-ω turbulence model provided the best predictions. At lower NPRs, due to the strong three-dimensional effects caused by shocks (observed in experimental results), two-dimensional predictions were inadequate. Verma et al.[22, 23] based on Hunter's experimental model, conducted experimental studies on three planar nozzles with different wall divergent angles and the same area ratio, designed for a Mach number of 2. They found that the boundary layer type and nozzle wall divergent angle had a significant impact on nozzle asymmetric flow. With a constant area ratio, increasing the divergent angle prevented asymmetric flow. When the divergent angle was 5.7°, RSS always appeared on the lower wall of the nozzle, and FSS appeared on the upper wall. When the nozzle divergent angle was 10.5°, the phenomenon of asymmetric flow was absent. Larger divergent angles made asymmetric flow less likely to occur.

These studies indicate that when a convergent-divergent nozzle is in an over-expanded state, flow separation occurs, leading to unpredictable asymmetric separation. Due to its unique curved configuration and round-to-square cross-section design, the serpentine nozzle experiences complex pressure gradients and strong swirl characteristics, resulting in non-uniform jet parameter distribution.

These complex flow phenomena can couple with flow separation under over-expanded state, causing the serpentine convergent-divergent nozzle to exhibit different flow characteristics compared to conventional convergent-divergent nozzles, thus facing greater challenges. It is necessary to conduct research on the flow separation characteristics of serpentine convergent-divergent nozzles under over-expanded state, to provide guidance for the design and flow separation control of serpentine convergent-divergent nozzles. Using the experimental platform of the Jet Propulsion Theory and Engineering Laboratory at Northwestern Polytechnical University, cold-state model experiments were conducted on the serpentine convergent-divergent nozzle at NPRs ranging from 1.4 to 3.0. Corresponding numerical investigation on the serpentine convergent-divergent nozzle were carried out in order to obtain the flow separation mechanism.

2. Experimental and Numerical Arrangement

2.1 Test facility

The experimental investigation was conducted on a flow exhaust system at Northwestern Polytechnic University, as shown in Figure 1. The test facility consists of a high-pressure air tank, a mainstream system, a static pressure measurement system, a six-component balance system and a schlieren system.

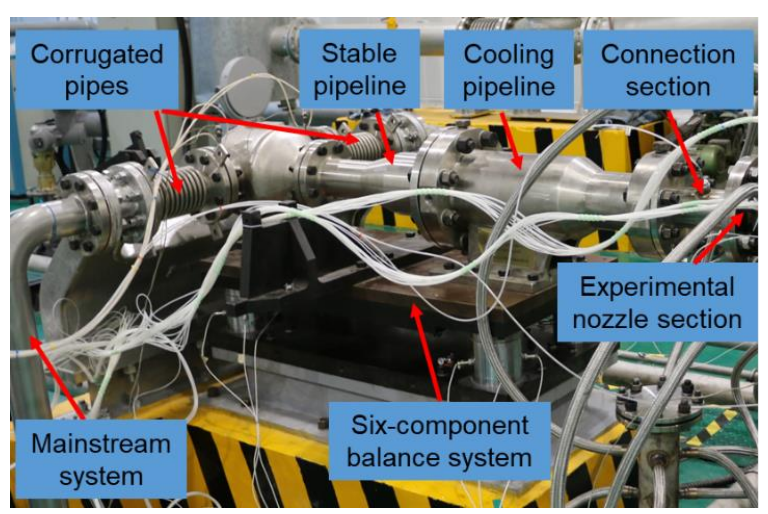


Figure 1 The flow exhaust system

The mainstream system is composed of a mass flow meter, an electric regulating valve, two corrugated pipes, a stable pipeline, a cooling pipeline, a connection section and an experimental nozzle section. The range of the mainstream mass flow rate is 0–4kg/s, and the accuracy of the mass flow measurement device is 1.0%. The mainstream system utilizes a design with a circumferential inlet configuration. This design choice is made because a circumferential inlet does not introduce extra axial forces during the experiment, thereby minimizing the potential for measurement inaccuracies in determining the nozzle's axial force.

The test system consists of a six-component balance system, a schlieren system and a static pressure test system. The six-component balance system is utilized to detect and measure the force exerted on the six components simultaneously. In space, forces decompose into three forces (F_x , F_y , F_z) and three moments (M_x , M_y , M_z) in a coordinate system. The range of thrust in X direction is 0–6kN, and the range of rolling torque is 0–1kN·m. The range of lift in Y direction is 0–3kN, and the range of yaw torque is 0–2kN·m. The range of lateral force in Z direction is 0–2kN, and the range of pitching torque is 0–3kN·m. The static calibration accuracy of the balance is 1.5% F.S. The PSI electronic pressure scanning valves (as shown in Figure 2) are employed for pressure measurement with totally 80 channels, and the measurement accuracy is 0.05%. The schlieren system captures the flow field's external shock structure, comprising a main reflector, light source slit concentrator, plane mirror, and knife-edge camera systems, as shown in Figure 3.



Figure 2 The PSI electronic pressure scanning valves.

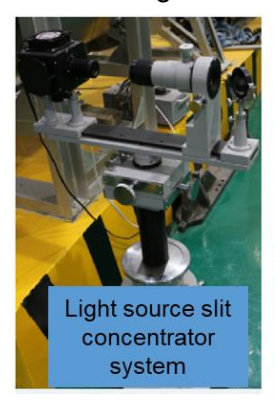








Figure 3 The schlieren system

2.2 Experimental nozzle and conditions

The design parameters of the serpentine convergent-divergent nozzle model are shown in Figure 4. and Table.1. The serpentine convergent-divergent nozzle consists of a serpentine convergent section, and a two-dimensional divergent section. The serpentine convergent section is designed based on a variable cross-sectional area pipeline design method that incorporates multiple parameters. It includes the first bend and the second bend. The convergent section is composed of a centerline and a series of cross-sections distributed along this centerline. The centerline is constructed using the Lee curve equation, with the cross-sections transitioning from a circular inlet cross-section to a rectangular outlet cross-section. The inlet of the divergent section connects to the outlet of the serpentine convergent section, forming the throat of the serpentine convergent-divergent nozzle. The width of the divergent section is uniform, indicating that it only extends in the direction parallel to the flow. The main design parameters are nozzle inlet diameter D, inlet area A_7 , axial length of the first bend L_1 , longitudinal deflection ΔY_1 , outlet area A_{71} , axial length of the second bend L_2 , longitudinal deflection ΔY_2 , throat area A_8 , throat width/height ratio W_8/H_8 , axial length of the divergent section L_3 , outlet area A_9 , and divergent angle β . This design parameter corresponds to a design NPR of 7.7 and a design Mach number of 2.0.

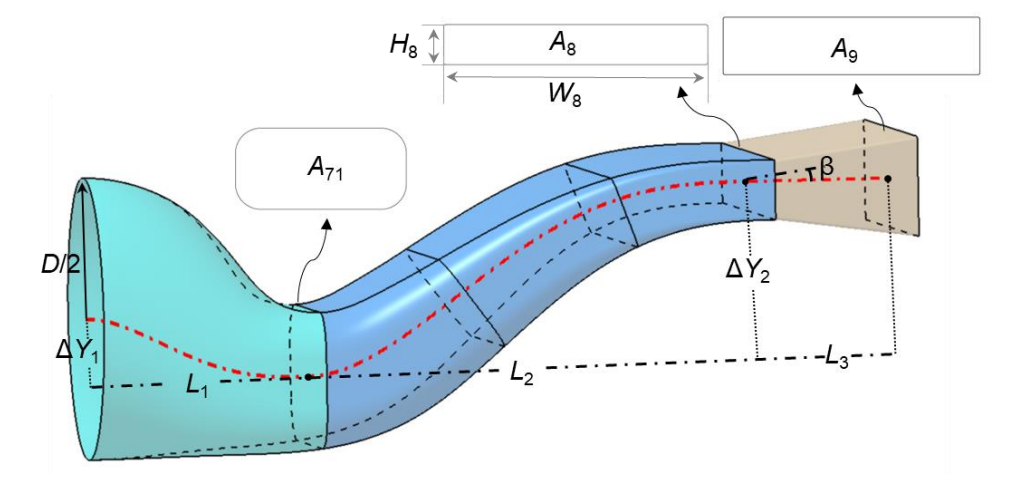


Figure 4 The design parameters of the serpentine convergent-divergent nozzle

Table 1 The parameter values

Parameters	Value/mm	Parameters	Value
D	40	A ₇₁ /A ₇	0.6
ΔY_1	17.8	A_8/A_7	0.4
ΔY_2	52.5	A_9/A_8	1.7
L_1	63.6	W_8/H_8	7
L_3	41.0	L_2/L_1	2
		β	7.8°

Static pressure orifices are installed on the nozzle walls to measure the gauge static pressure inside the nozzle. As shown in Figure 5, three rows of static pressure orifices are distributed to the upper wall, lower wall, and side wall, respectively. Each row has 10 static pressure orifices in the serpentine convergent section, while the divergent section has 11 static pressure orifices on both the upper and side walls, and 12 static pressure orifices on the lower wall. The experimental model is shown in Figure 6. The nozzle is made of 304 stainless steel, with a wall thickness of 5 mm to prevent deformation and vibration that could affect the internal flow. The nozzle inlet is connected to a flange for easy installation. The flange has evenly spaced holes to avoid uneven wall stress, which could affect the accuracy of thrust measurements. Static pressure taps are inserted into the static pressure orifices and sealed with sealant. These taps are connected to the PSI electronic pressure scanning valves to measure the gauge static pressure.

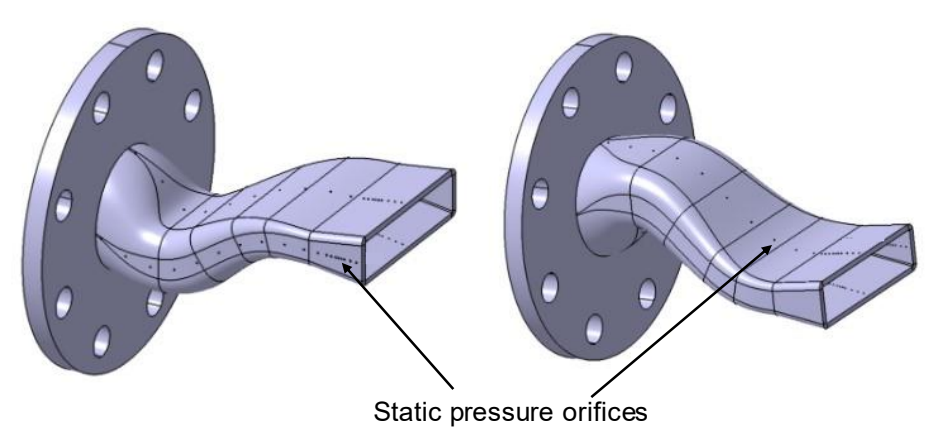


Figure 5 The distribution of static pressure orifices



Figure 6 The experimental model

Twelve total-pressure taps were positioned at the connection section of the mainstream system. The total pressure at the nozzle inlet is adjusted by changing the opening degree of electric regulating valve, in order to achieve different NPRs. During the experiment, the atmospheric pressure and temperature was measured to be 95285Pa and 302.65K, and the temperature of the gas in the high-pressure air tank was measured to be 307.15K, which is used as the total temperature at the nozzle inlet. Experimental data, including schlieren photographs, gauge static pressure, mass flow and thrust,

were acquired at various NPRs between 1.4 and 3.0.To ensure the reliability of the experiments, the PSI electronic pressure scanning valves was checked and calibrated with a standard pressure measuring instrument, while the temperature sensor was verified and calibrated using standard temperature measuring equipment. Several experiments were conducted and the results were compared. The comparison revealed high consistency in static pressure and schlieren photographs among the experiments, thus minimizing the potential for random errors.

2.3 Numerical Modeling

The commercial software ANSYS FLUENT was used to perform numerical simulations of the flow field within the serpentine convergent-divergent nozzle. The three-dimensional steady-state compressible Reynolds-Averaged Navier-Stokes (RANS) equations were solved using a pressure-based coupled solver. The SST k-ω turbulence model was selected for the turbulence simulation. Second-order upwind schemes were used for spatial discretization, and the fluid was assumed to be an ideal gas. The structured grid and computational boundary conditions of the serpentine convergent-divergent nozzle is shown in the Figure 7. The nozzle profile is identical to the internal profile of the experimental nozzle. A 80 mm straight section was added in front of the nozzle inlet to stabilize the jet. Due to the 5 mm wall thickness of the experimental nozzle, which is non-negligible relative to the nozzle exit height, it was found in numerical simulations that this thickness affects the flow separation structure within the nozzle. Therefore, the influence of wall thickness was considered in the numerical simulation. The ambient zone extended approximately 20 inlet diameters downstream of the nozzle exit and 10 inlet diameters normal to the jet.

The grid in the divergent section was refined overall to capture the boundary layer separation and the formation of wave systems. The mesh near the nozzle wall was locally refined, with the height of the first layer of the grid ensuring $y^+<1$ to meet the computational requirements of the SST k- ω turbulence model. According to local experimental conditions, the back pressure p_0 is 95285 Pa. A pressure-inlet boundary was used at the nozzle inlet, with the inlet total pressure p_0^* determined based on the NPR, and the inlet total temperature $T^* = 307.15$ K. The far-field inlet boundary and surrounding boundaries were set as pressure-far-field boundaries, with a far-field Mach number $Ma_\infty=0.02$ Ma, a far-field static pressure $p_0=95285$, and a far-field static temperature $T_0=302.65$ K. The far-field outlet was set as a pressure-outlet boundary. The nozzle wall was treated with no-penetration, no-slip, and adiabatic wall boundary conditions to ensure that the normal fluxes of mass, momentum, and energy on the wall surface were zero.

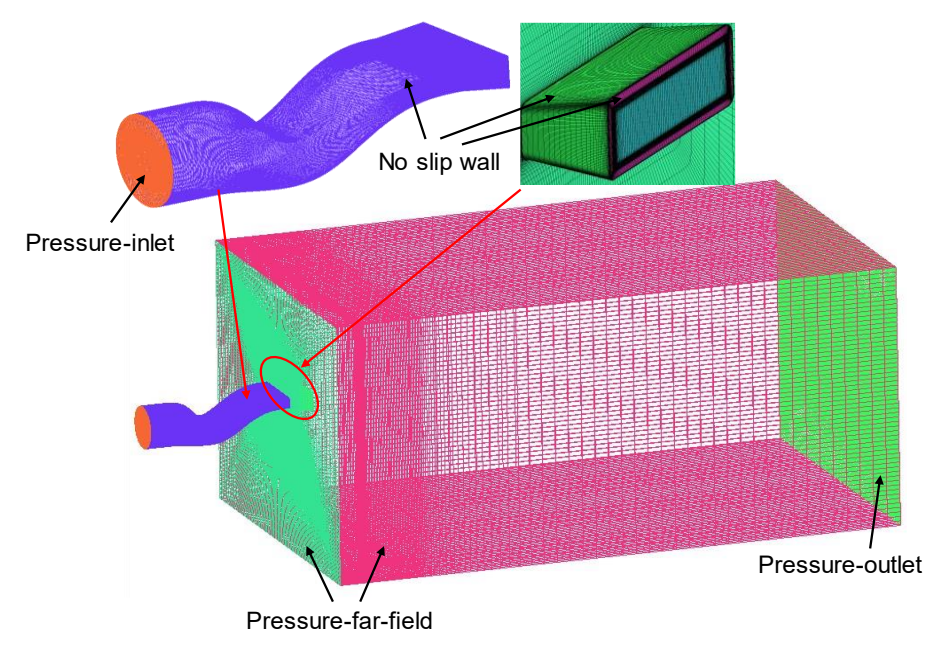


Figure 7 The structured grid and computational boundary conditions

3. Results and discussions

The experimental and numerical investigation results are analyzed in detail to reveal the flow separation mechanism of the serpentine convergent-divergent nozzle under over-expanded state. Schlieren photographs at different NPRs are shown in Figure 8. The results show that the jet is deflected upward at low NPRs stably. When the NPR is 1.4, a distinct jet boundary appears on the upper side of the jet, indicating the presence of a viscous shear layer caused by the velocity difference across the boundary, known as the velocity shear layer. As the NPR increases, the velocity shear layer on the lower side of the jet begins to appear and gradually thickens. With further increases in the NPRs, two velocity shear layers start to emerge at the center of the jet, positioned closer to the upper velocity shear layer. At NPRs of 2.1 and 2.2, the wave systems begin to form on the lower side of the jet, connecting to both the central and lower velocity shear layers. When the NPR reaches 2.45, the wave systems appear on the upper side of the jet, connecting to both the central and upper velocity shear layers. Additionally, the wave systems are observed between the two central velocity shear layers, which seem to interact with the upper and lower wave systems, resulting in a complex wave system. The wave systems on the upper and lower sides are asymmetry. At a NPR of 2.6, the wave systems on the upper and lower sides become approximately symmetry, and the two central velocity shear layers become more distinct. As the NPR continues to increase, the distance between the two central velocity shear layers shortens. At a NPR of 3.0, the upper and lower velocity shear layers change from a double-linear shape to a "gourd" shape.

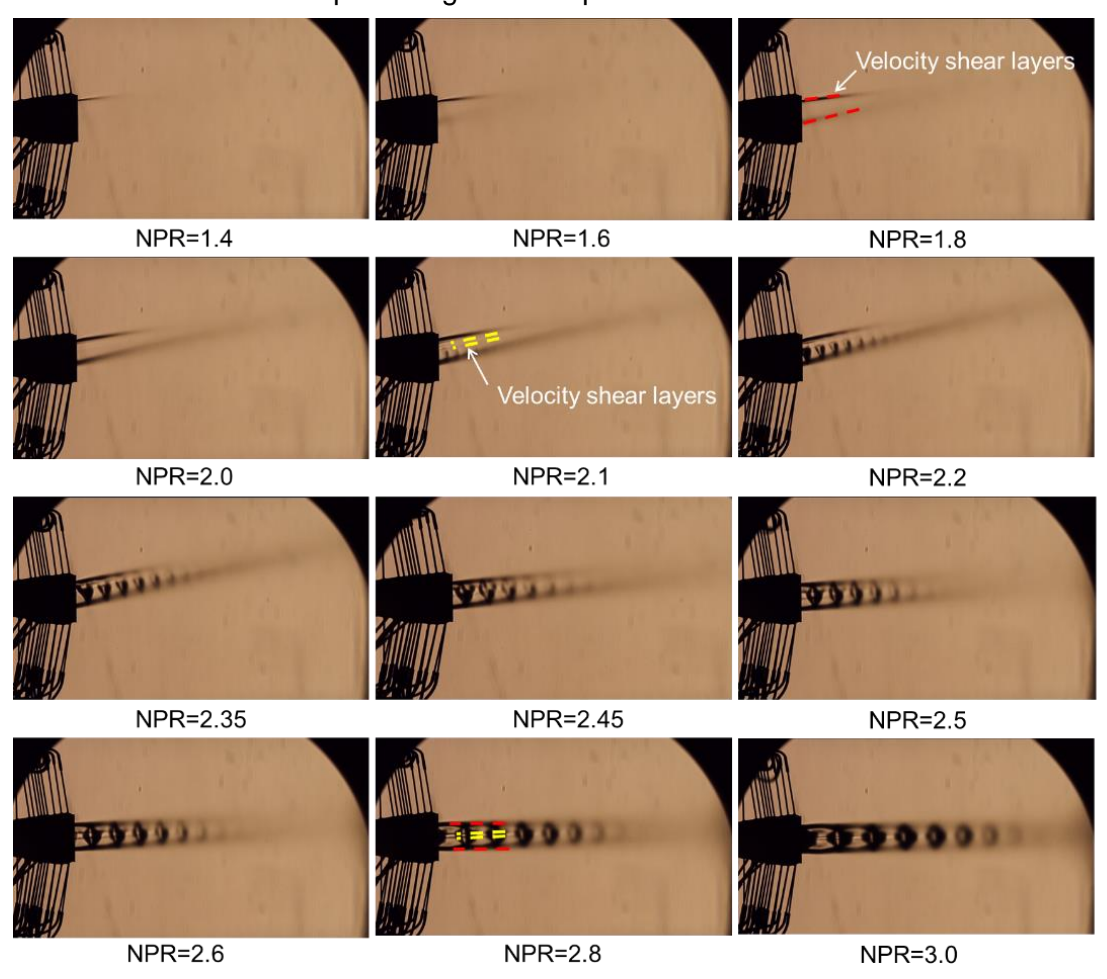


Figure 8 The schlieren photographs at different NPRs

Compare the numerical simulation results with the experimental results at the same NPR, as shown in the Figure 9. It is found that the experimental schlieren photographs and the numerical schlieren images match very well at different NPRs. The velocity shear layers in the experimental schlieren system coincide highly with the positions of the shear layers in the numerical schlieren images, including the upper and lower velocity shear layers as well as the central velocity shear layer. The

distribution of wall gauge static pressure in the experiments aligns closely with the distribution of wall gauge static pressure extracted from the numerical simulations, with a maximum error not exceeding 5%. The numerical simulations can accurately capture the point where the wall gauge static pressure starts to rise in the divergent section. It can be seen that numerical simulations can accurately predict the flow separation structure within the serpentine convergent-divergent nozzle. Additionally, a double "λ" shock structure was observed in the numerical schlieren images, consisting of an incident shock, a reflected shock, and a central Mach stem. This shock structure is closely related to the flow separation structure within the nozzle and determines the schlieren structure outside the nozzle. Due to the opaque divergent section of the experimental model, the internal shock structure could not be observed. A detailed analysis and discussion of the internal flow structure at different NPRs will be conducted below, combining numerical simulation and experimental results, to elucidate the reasons for the observed flow phenomena in the serpentine convergent-divergent nozzle under over-expanded state.

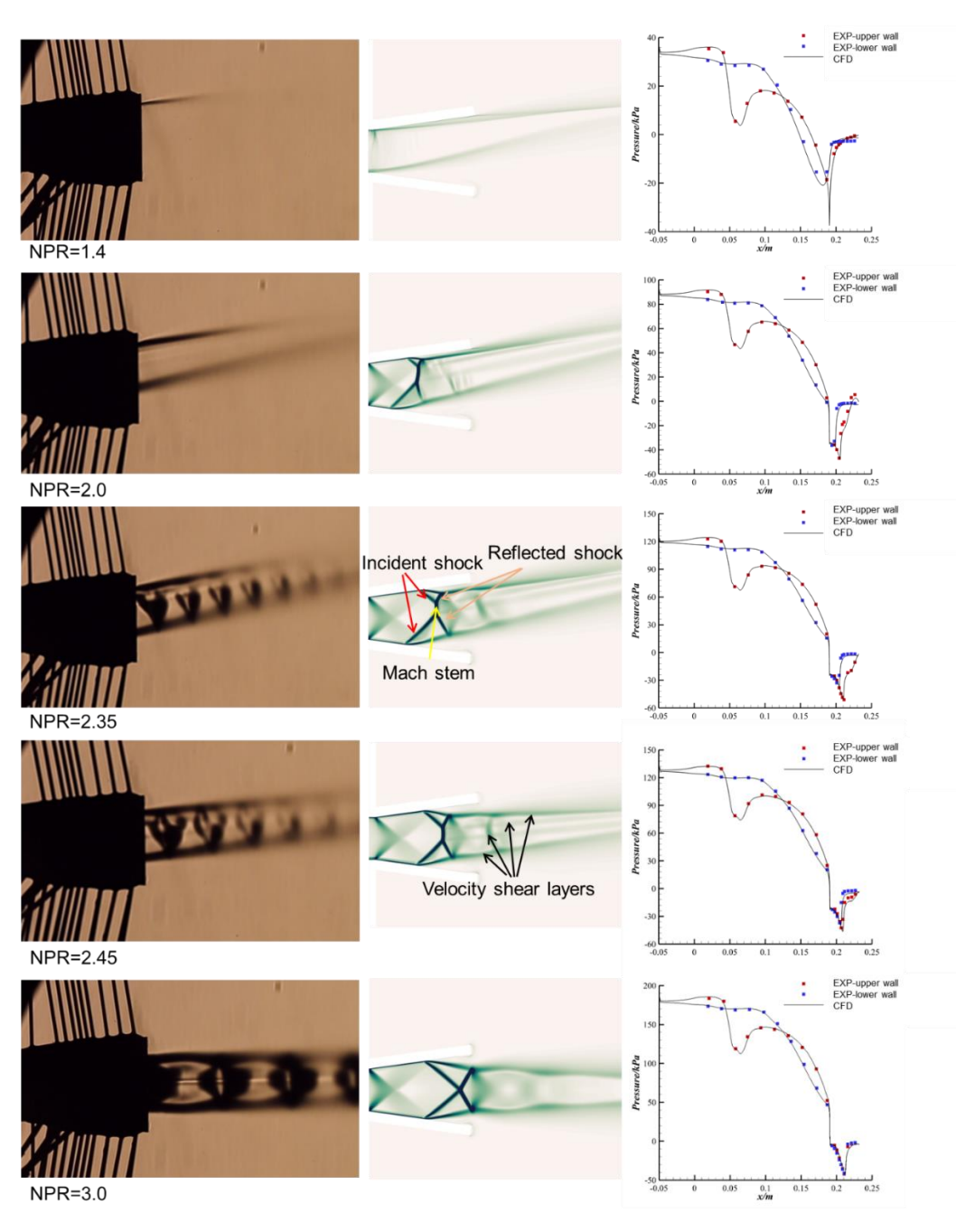


Figure 9 Comparation of the numerical simulation and the experimental results

The Figure 10 shows the Mach number and streamline on the vertical symmetry plane at different NPRs. At a NPR of 1.4, a large area of flow separation occurs on the lower side of the divergent section. This flow separation is connected to the external atmosphere and is referred to as FSS. The separation affects the distribution at the throat position, with the Mach number exceeding 1 only at the upper corner. The flow adheres to the upper wall of the nozzle, resulting in a large velocity gradient at the upper wall exit, which can be observed as a distinct velocity shear layer in the schlieren system. The jet on the lower side mixes with the atmosphere within the nozzle, causing the velocity shear layer on the lower side at the exit to thicken and the gradient to decrease, making it unobservable in the schlieren system.

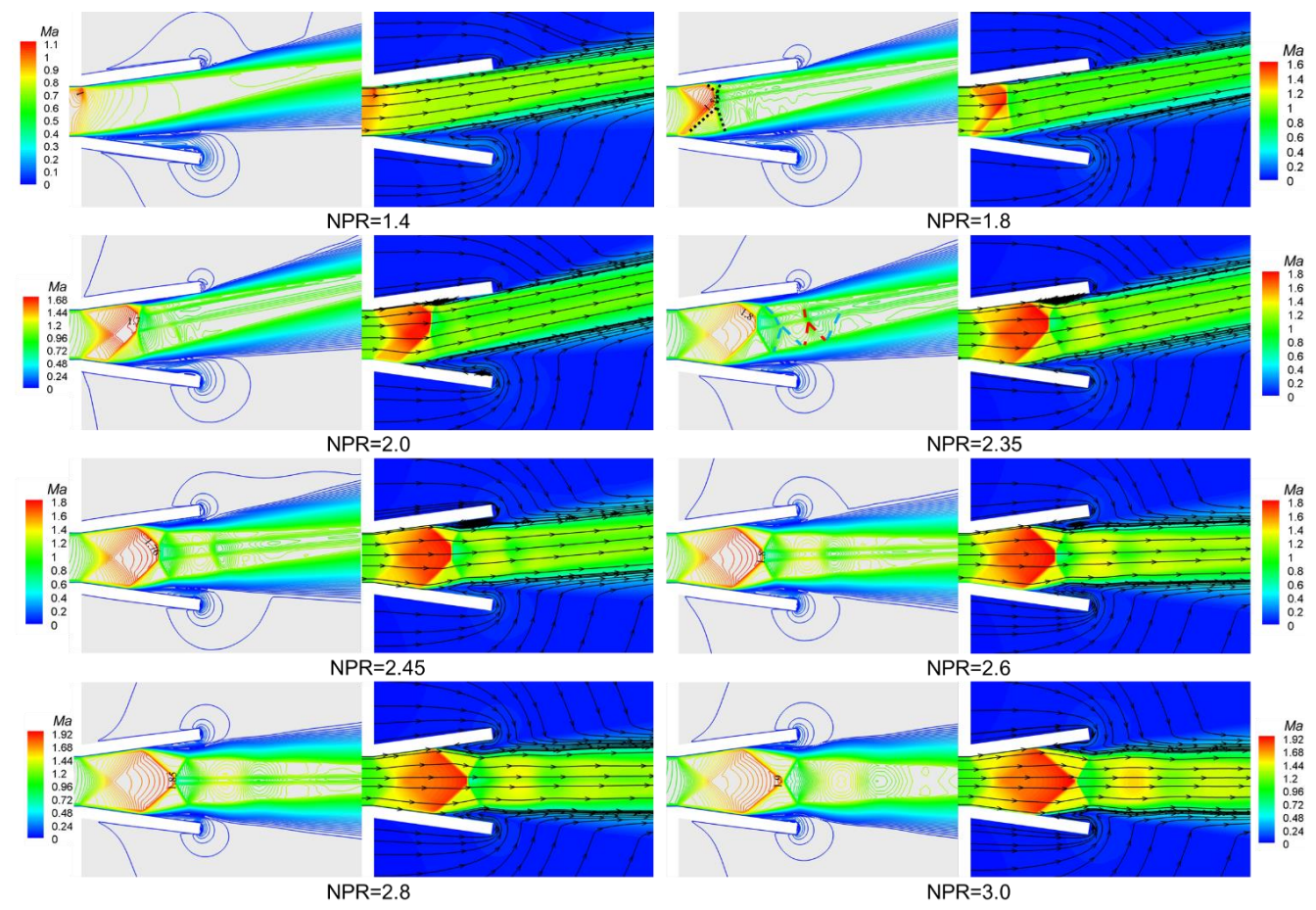


Figure 10 Mach number and streamline on the vertical symmetry plane at different NPRs

As the NPR increases, the flow separation region on the lower side decreases, and the velocity gradient on the lower side at the exit increases, becoming gradually observable in the schlieren system. The velocity shear layer on the lower side is significantly thicker than the upper side, due to the internal and external flow mixing effects within the nozzle. At a NPR of 1.8, an asymmetric double "\u03b4" shock structure appears within the divergent section. After the incident shock is generated, the boundary layer airflow can't resist the pressure rise, leading to flow separation. Therefore, the incident shock results from shock/boundary layer interaction under the influence of flow separation. The central Mach stem is a stronger shock that significantly reduces the jet speed to balance the back pressure, while the reflected shock redirects the jet. The strengths of the upper shock, central Mach stem, and lower shock differ, resulting in significant velocity differences after the jet passes through the double "λ" shock structure, forming stratified flow and creating two central velocity shear layers. Due to the smaller size of the upper "λ" shock structure, the two central velocity shear layers are closer to the upper side. The velocity shear layer can be considered the virtual boundary of the jet. Between the central velocity shear layer and the lower velocity shear layer, the reflected shock of the "λ" shock structure continues to reflect due to the influence of the shear layer "boundary," leading to the appearance of a series of wave systems. The intensity and range of the upper "λ" shock structure are

smaller than those of the lower one, so the wave systems on the lower side is observed first in the schlieren system.

At a NPR of 2.0, a clear RSS can be observed on the upper side of the divergent section. After flow separation, the jet continues to adhere to the wall and does not connect with the external atmosphere. As the NPR increases, the upper " λ " shock structure gradually enlarges, and the RSS moves rearward and expands in size. At a NPR of 2.45, the upper RSS is pushed out of the nozzle and connects with the atmosphere, transforming into FSS. The differences in shock structure between the upper and lower sides rapidly diminish, and during the experiment, noticeable jumps in jet deflection can be observed. Additionally, the wave systems on the upper side begins to be seen in the schlieren system. As the NPR continues to increase, the double " λ " shock structure gradually becomes symmetrical, and the jet gradually levels out. The intensity of the shocks increases, the shock structure moves closer to the exit, and the central velocity shear layer and shock reflection system become more prominent in the schlieren system. When the NPR is 3.0, due to the appearance of alternating shock waves and expansion waves in the jet, the shear layer transforms into a "gourd" shape.

Figure 11 shows the gauge static pressure along the centerline of the upper and lower walls of the divergent section measured by the PSI electronic pressure scanning valves at various NPRs. Figure 12 shows the corresponding numerical simulation results of the gauge static pressure on the vertical symmetrical plane at the same NPRs. It can be observed that the incident shock causes a sudden increase in static pressure, leading to a corresponding increase in static pressure along the centerline of the nozzle wall. Influenced by the asymmetric double " λ " shock structure, the positions of the incident shock on the upper and lower sides are different. At low NPR, the position of the incident shock on the lower side is noticeably further forward, causing the location of increased static pressure on the lower nozzle wall to be ahead of that on the upper wall. When the NPR is 1.8, the static pressure on the upper wall slowly increases past the turning point, exceeding the ambient pressure before slightly decreasing. This occurs because the centerline of the upper wall passes through the incident shock and first enters the RSS region, where the static pressure is significantly lower than the static pressure after the jet attaches to the wall, resulting in a slow pressure increase. Due to the influence of the wave system, there is a local maximum static pressure point near the upper wall exit, causing the centerline static pressure to exceed the ambient pressure before the exit. On the lower wall centerline, the static pressure rapidly increases to near atmospheric pressure after passing through the incident shock and remains constant, characteristic of the FSS.

At a NPR of 2.0, the position where the static pressure starts to increase on both the upper and lower walls moves further backward compared to when the NPR is 1.8. Due to the proximity of the exit, only localized high pressure regions are captured, so the static pressure on the upper wall shows a distribution that always increases and exceeds the atmospheric pressure. At a NPR of 3.5, the RSS-FSS structure remains unchanged, and the static pressure variation trend on both the upper and lower walls remains basically the same. The wave systems of the jet is simple, without forming complex reflections near the walls. The static pressure on the upper wall after the incident shock changes more uniformly, and the static pressure before the exit remains below ambient pressure. When the NPR is 2.45, the position where the static pressure on the upper wall starts to increase moves slightly forward. This is because the RSS on the upper side transforms into FSS. The external airflow impacts the jet, rapidly reducing the size difference between the shocks on the upper and lower sides, causing the separation position on the upper wall to move forward. The static pressure change trend on both the upper and lower walls is consistent, but the static pressure on the upper wall is still lower than that on the lower wall. As the NPR continues to increase, the position where the static pressure starts to increase on both walls moves further backward and the separation positions gradually get closer. The static pressure at the exit position on the upper wall gradually increases with the NPR due to the overall backward movement of the shock structure position and the gradual symmetry of flow separation. When the NPR is 3.0, the positions where the static pressure starts to increase on both the upper and lower walls are the same, indicating symmetrical flow separation. Overall, the position where the static pressure on the lower wall starts to rise moves backward with the increase in NPR. The position where the static pressure on the upper wall starts to increase first moves backward with the increase in NPR. then suddenly moves forward when the upper RSS transforms into FSS, and subsequently continues to move backward with the further increase in NPR.

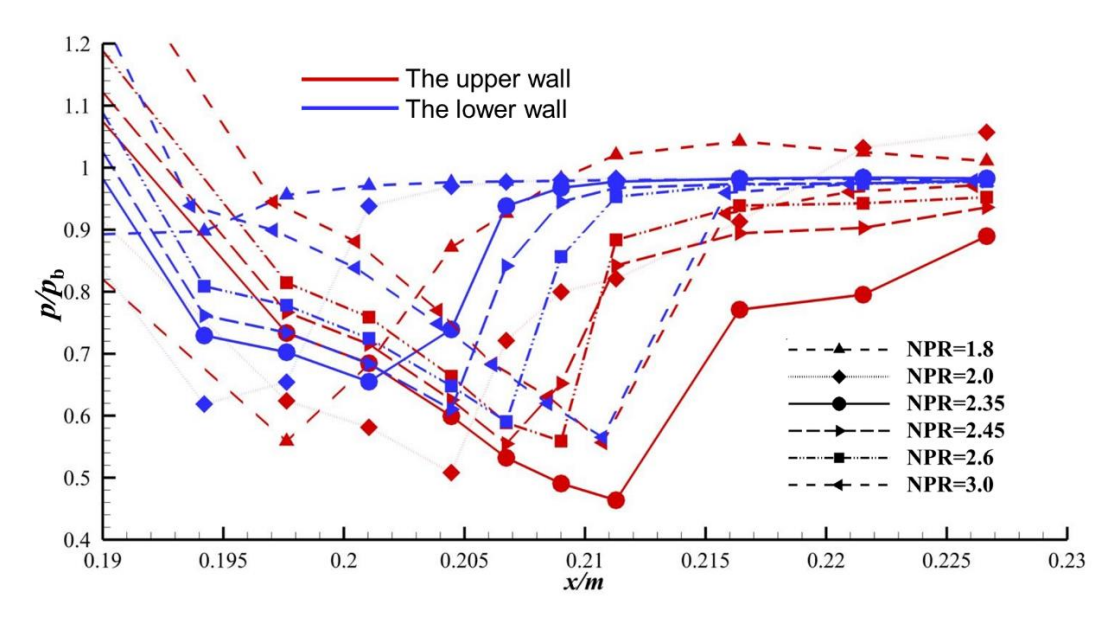


Figure 11 The gauge static pressure measured along the centerline of the upper and lower walls of the divergent section

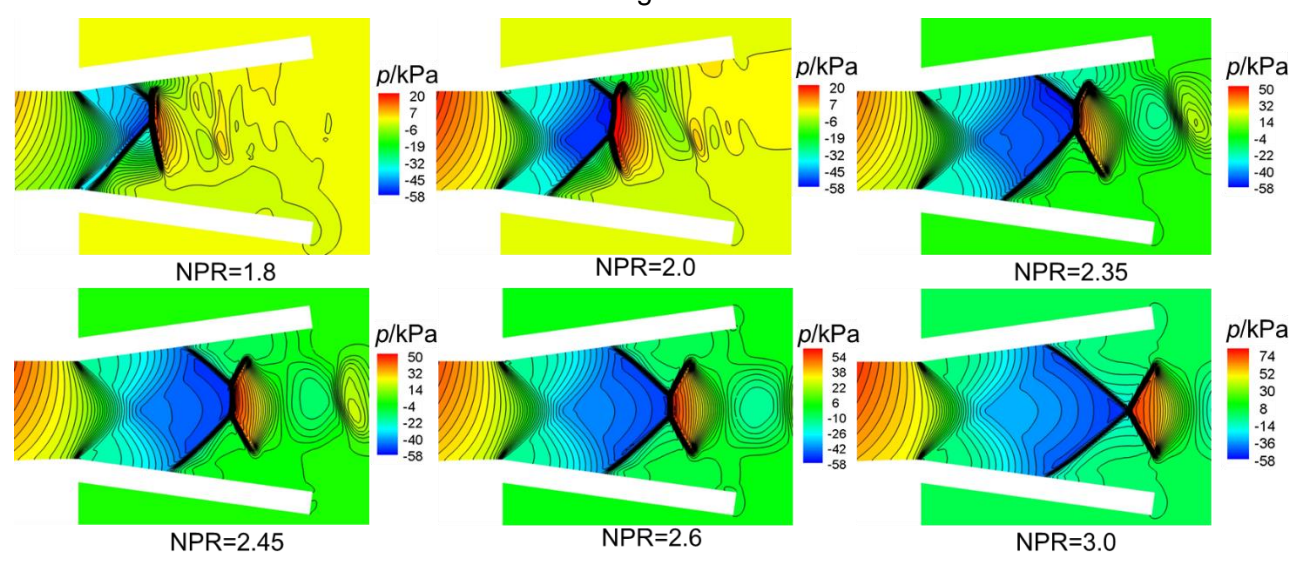


Figure 12 The gauge static pressure on the vertical symmetrical plane of numerical simulations

Figure 13 shows a comparison of the gauge static pressure along the centerline of the side wall and upper and lower walls of the divergent section measured by the PSI electronic pressure scanning valves at various NPRs. Figure 14 shows the gauge static pressure across different sections at corresponding NPRs of numerical simulations. Section 1 is defined as the vertical symmetry plane of the nozzle, Section 2 as the vertical plane near the side wall of the divergent section, Section 3 as the vertical plane located $0.35\,W_8$ away from the vertical symmetry plane, and Section 4 as the horizontal symmetry plane of the divergent section.

At a NPR of 1.4, the static pressure variation of the jet is relatively uniform, with the static pressure along the centerline of the side wall falling between those of the upper and lower walls. When the NPR is 1.8, besides the appearance of a double " λ " shock structure in Section 1, an incident shock is also observed in Section 4 resulting from the interaction between the shock and the boundary layer on the side wall. The shock structure within the vertical and horizontal planes interact, leading to the three-dimensional nature of the shocks within the nozzle. In Section 4, two shock lines appear due to the passage through the incident and reflected shocks, but they merge into a single line near the side wall.

Consequently, the length of the central normal shock in Section 3 is greater than that in Section 1. The starting positions of the incident shocks on the upper and lower sides are ordered as Section 2 > Section 3 > Section 1. Due to the influence of shocks in the horizontal plane, the central normal shock in the vertical plane moves forward near the side wall, closer to the starting position of the upper incident shock. Therefore, at the side wall, the upper incident shock and the central Mach stem form a new normal shock and the shock structure in Section 2 becomes a combination of an upper normal shock and a lower oblique shock. The sudden increase in static pressure detected by the static pressure taps on the side wall reflects both the position of the central shock in Section 2 and the starting position of the incident shock in Section 4. The sudden increase in static pressure on the upper and lower walls indicates the starting positions of the upper and lower incident shocks in Section 1. Due to the effects of wall viscosity and the three-dimensional nature of the shocks, the position of the upper incident shock in Section 1 is further forward than that of the lower incident shock, and the position of the upper incident shock is close to the position of the normal shock in Section 2. Therefore, the positional order of increase in static pressure is lower wall > upper wall ~ side wall.

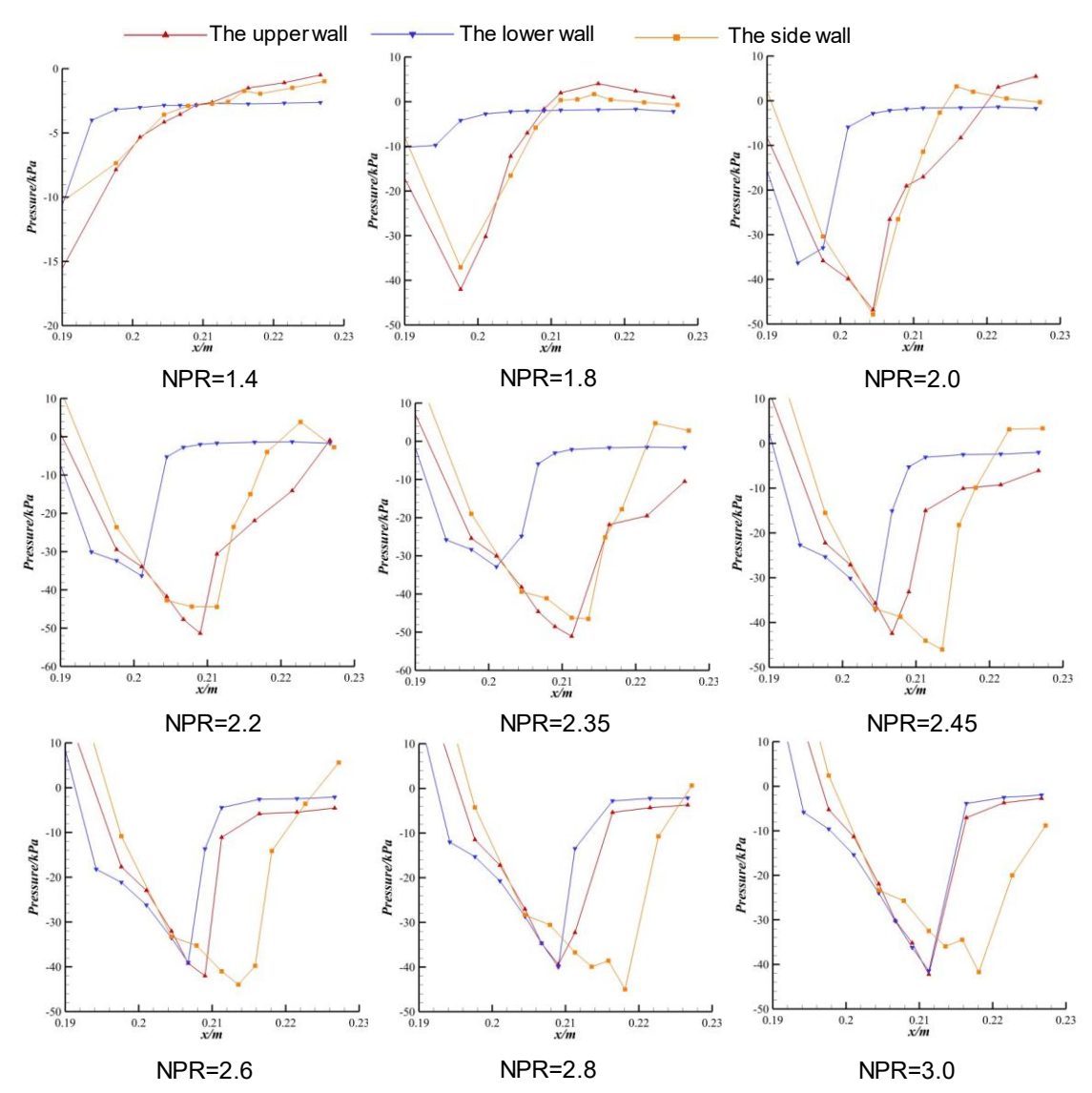


Figure 13 The gauge static pressure of the divergent section measured by the PSI electronic pressure scanning valves

At a NPR of 2.0, the static pressure variation trend is similar to that at a NPR of 1.8. The two shock lines in Section 4 are closer together and again merge into a single shock line near the side wall. A significant reflected shock can be observed in Section 4, presenting a double " λ " shock structure. However, the central Mach stem of the double " λ " shock structure is very long, and the incident and

reflected shock are relatively small and generated only near the sidewall surface. When the NPRs are 2.2 and 2.35, the two shock lines in Section 4 are completely separated, and the shock structure in Sections 1 and 3 are nearly identical. The starting position of the normal shock on the upper side of the Section 2 is moved backward by an increased distance, so the position where the static pressure begins to increase along the centerline of the side wall is behind that of the upper wall significantly. At NPRs of 2.45 and 2.6, Section 4 passes through the central Mach stem, so the two shock lines become a single shock line. Due to the enlargement of the upper "λ" shock structure, the shock structures in Section 2 changes to two asymmetrical oblique shocks and a central normal shock and the distance between the position of the upper incident shock in Section 2 and that in Section 1 increases. The pressure ahead of the central normal shock in Section 2 is lower than the pressure ahead of the central Mach stem in Section 1. Therefore, the position where the static pressure starts to increase along the centerline of the side wall is further back compared to the upper wall, with a lower pressure before the increase.

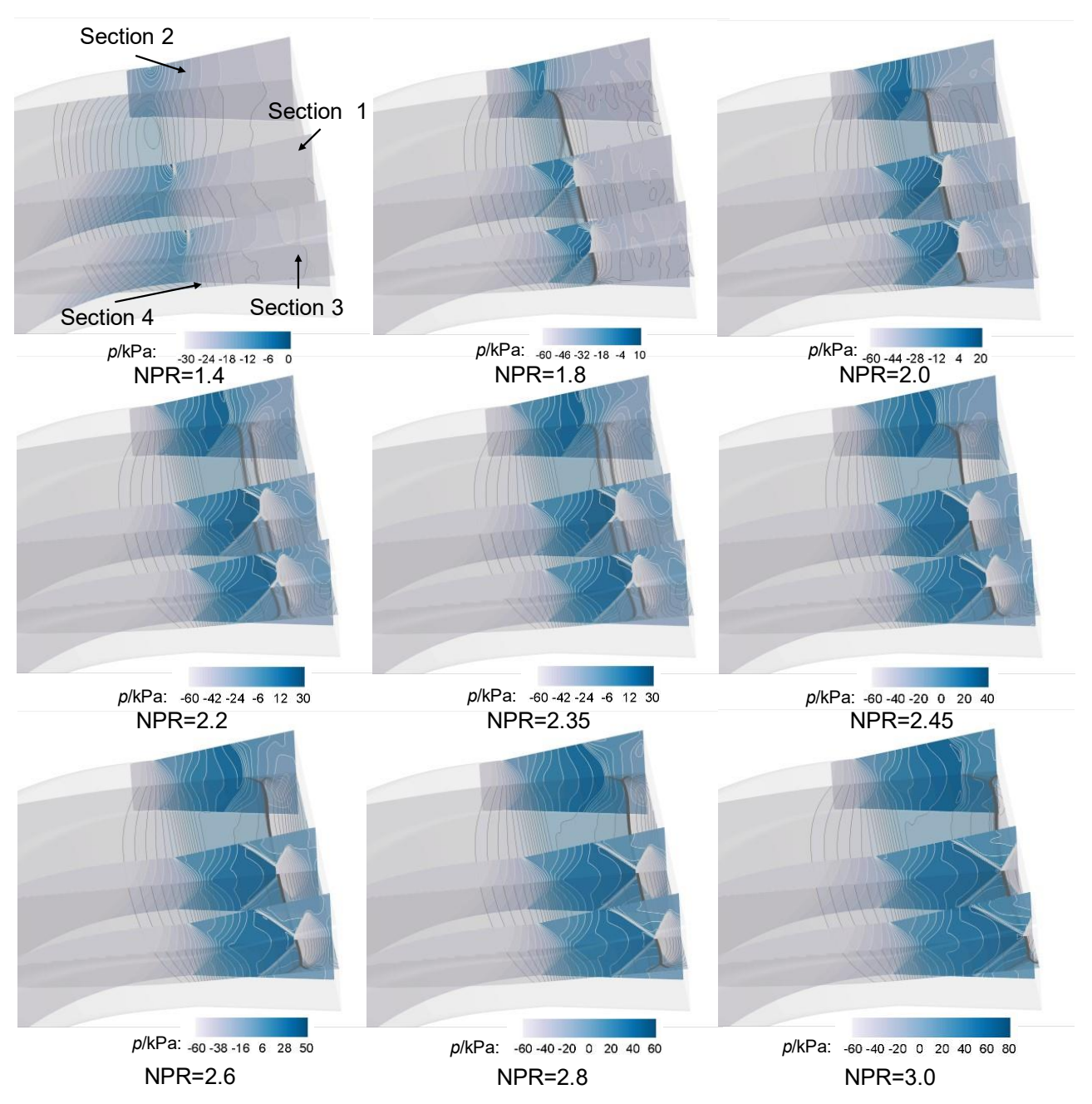


Figure 14 The gauge static pressure across different sections of numerical simulations

At a NPR of 3.0, the positions where the static pressure starts to increase along the centerlines of the upper and lower walls are the same and move further backward compared to those at a NPR of 2.8, indicating a nearly symmetrical jet. However, the position where the static pressure starts to increase along the side wall remains almost the same as at a NPR of 2.8. This is due to the increased incident shock of the " λ " shock structure in Section 4. Additionally, under the combined influence of shocks in different dimensions, the differences among Sections 1, 2, and 3 increase, and the three-dimensional nature of the jet becomes more pronounced. The bending of the central Mach stem in Section 4 increases, and the hysteresis of the shock structures near the side wall relative to the central increases. The length of the central Mach stem in Section 2 significantly increases.

To investigate the reasons for the flow separation structure in the serpentine convergent-divergent nozzle, a detailed analysis of the internal flow field at a NPR of 2.35 was conducted. Figures 15 and 16 shows the static pressure, streamline, and the Mach number on the vertical symmetry plane and various cross-sections along the path of the nozzle. Section A is located at the inlet of the serpentine convergent section, Section B at the first bend, and Section E at the second bend. Sections C and D are located between the first and second bends. Section F is located at the throat. Sections G, H and I are within the divergent section. At this NPR, Section G is located before flow separation occurs, Section H is where the upper side experiences no flow separation but the lower side experiences FSS, and Section I is where RSS occurs on the upper side.

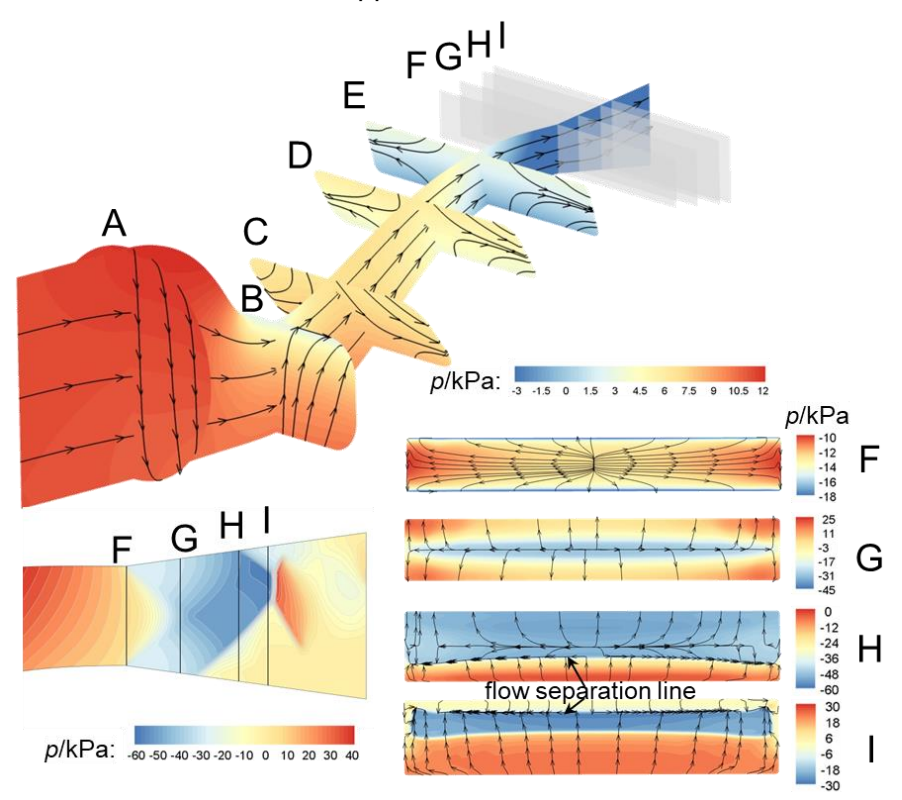


Figure 15 The gauge static pressure and streamline on the vertical symmetrical plane and various cross-sections along the path of the nozzle

It can be observed that the serpentine curved duct has a complex configuration with significant changes in flow curvature, resulting in notable internal flow non-uniformity. Upon entering the serpentine duct, due to the overall downward curvature of the duct, the airflow in the upper part of the duct is compressed, leading to a decrease in Mach number and an increase in static pressure. This pressure gradient maintains the downward motion of the airflow, with secondary flow streamlines in Section A pointing downward. As the airflow passes through the first bend of the serpentine nozzle, the streamlines curve, requiring a pressure difference directed from the outer to the inner side of the bend to provide the centripetal force. At the first bend, the airflow velocity on the upper wall rapidly increases, causing a quick drop in static pressure and forming a local high-speed low-pressure region.

Under this pressure difference, the secondary flow streamlines in Section B point upwards overall. Due to the upward curvature of the second bend duct, the airflow trends upwards, while the duct contracts and the width-to-height ratio increases, causing the upper part of the fluid to flow downwards. Additionally, influenced by the round-to-square configuration, the downstream duct expands laterally, causing the airflow to flow sideways. Therefore, in Sections C to E, the upper part of the secondary flow streamlines points downward, the lower part points upward, and both parts bend towards the side walls.

At the second bend, the curvature center shifts to the lower side of the nozzle, similarly requiring a pressure difference directed from the outer to the inner side of the bend to provide centripetal force. However, the curvature at the second bend is smaller than that at the first bend, so a local low-pressure region does not form at the lower wall bend. The effect is that the acceleration of the lower part of the airflow is greater than that of the upper part, resulting in higher pressure on the upper side than the lower side, with Mach number isoclines connecting from the upper wall to the lower wall. However, the pressure difference generated by the smaller curvature is insufficient to completely alter the upward trend of the airflow streamlines caused by the upward duct. From Section E to Section F, the duct continues to expand laterally, and the curvature of the longitudinal bend gradually decreases, reducing the static pressure difference between the upper and lower sides at the same cross-section section. At Section F, upon entering the divergent section, the jet needs to flow upwards and downwards, causing the secondary flow streamlines to point from the center towards the periphery.

In the Mach number distribution diagram, obvious vortex distributions appear in the upper corners of Sections E and F. This is because the pressure on the side wall is greater than on the upper and lower walls, causing the near-wall fluid in the upper part to flow from the outside to the inside under the pressure difference, generating positive/negative vorticity in the left/right upper corners, respectively. The generation of vorticity accelerates the mixing of airflow, making the Mach number exhibit a noticeable vortex pattern. The lower corners of both sections also show a vortex pattern in the Mach number distribution, formed for the same reason as the upper corners, but with lower intensity due to the lower pressure on the lower side. The influence of corner vorticity extends downstream to Sections H and I, where the Mach number shows a concave pattern, increasing the complexity of the separated flow.

It is noteworthy that at section F, the Mach number and pressure on the upper and lower sides of the section are vertically asymmetric and laterally non-uniform. This indicates that the airflow at the entrance of the divergent section exhibits a vertical asymmetry and a lateral non-uniform trend. This is because the lateral expansion of the nozzle terminates at this point, and the flow on both sides has not yet reached the same Mach number as the central flow, and the overall airflow is still influenced by the longitudinal curvature of the second bend in the serpentine convergent section. The vertical asymmetry affects the deflection direction of the airflow in the divergent section, while the lateral nonuniformity affects the three-dimensionality of the flow separation structure in the divergent section. At section F, the Mach number on the lower side is significantly higher than that on the upper side, and the pressure is lower than that on the upper side. Although this non-uniformity decreases to some extent within the divergent section, the overall Mach number on the lower side remains higher, and the pressure remains lower than that on the upper side before flow separation occurs. The boundary layer thickness is influenced by the compression effect at high Mach numbers, becoming thinner. A thinner boundary layer is less capable of withstanding adverse pressure gradients, making it more prone to separation. The higher the Mach number, the more likely flow separation is to occur. Additionally, the higher the Mach number, the closer it is to the conditions required for the nozzle to generate a shock in order to equalize the back pressure. Under the combined effect of these factors, an incident shock first occurs on the lower side, leading to flow separation.

The different positions of the incident shock and the varying sizes and intensities of the upper and lower " λ " shock structure result from the differences between FSS and RSS. The formation of RSS and FSS is both a result of thermodynamic equilibrium and the creation of a stable flow separation structure. When the shock structure is too far forward, if FSS occurs on both the upper and lower sides, the long separation region is difficult to maintain stably. In contrast, the RSS-FSS structure, with attached flow on one side, is a stable flow separation structure. This flow separation structure causes

the upper " λ " shock structure to be smaller and the lower " λ " shock structure to be larger, with the central Mach stem closer to the upper side of the nozzle, achieving the effect of balancing the back pressure and deflecting the airflow. Therefore, it is evident that the RSS-FSS stable structure is responsible for the asymmetry of the flow separation, while the non-uniform inlet of the divergent section is responsible for the deflection of the jet fixed upwards. The lateral non-uniformity manifests in the central jet having a higher Mach number than the lateral sides, and the Mach number near the sidewalls being even lower. Consequently, flow separation first occurs at the center of the jet laterally, with a certain hysteresis in flow separation on both sides. This is the reason for the more backward position of the incident shock on both sides with respect to the center position in the vertical plane.

At section H, the secondary flow in the mainstream part moves from the center towards the upper and lower sides. A clear flow separation line formed by FSS can be observed on the lower side. This separated flow comes from the external atmosphere, resulting in a significantly higher pressure than the mainstream and a very low Mach number. At section I, a flow separation line formed by RSS can also be observed on the upper side. This separated flow comes from the mainstream after the shock, so its pressure is higher than that of the airflow in the middle position before the shock but much lower than the pressure of the separated flow on the lower side.

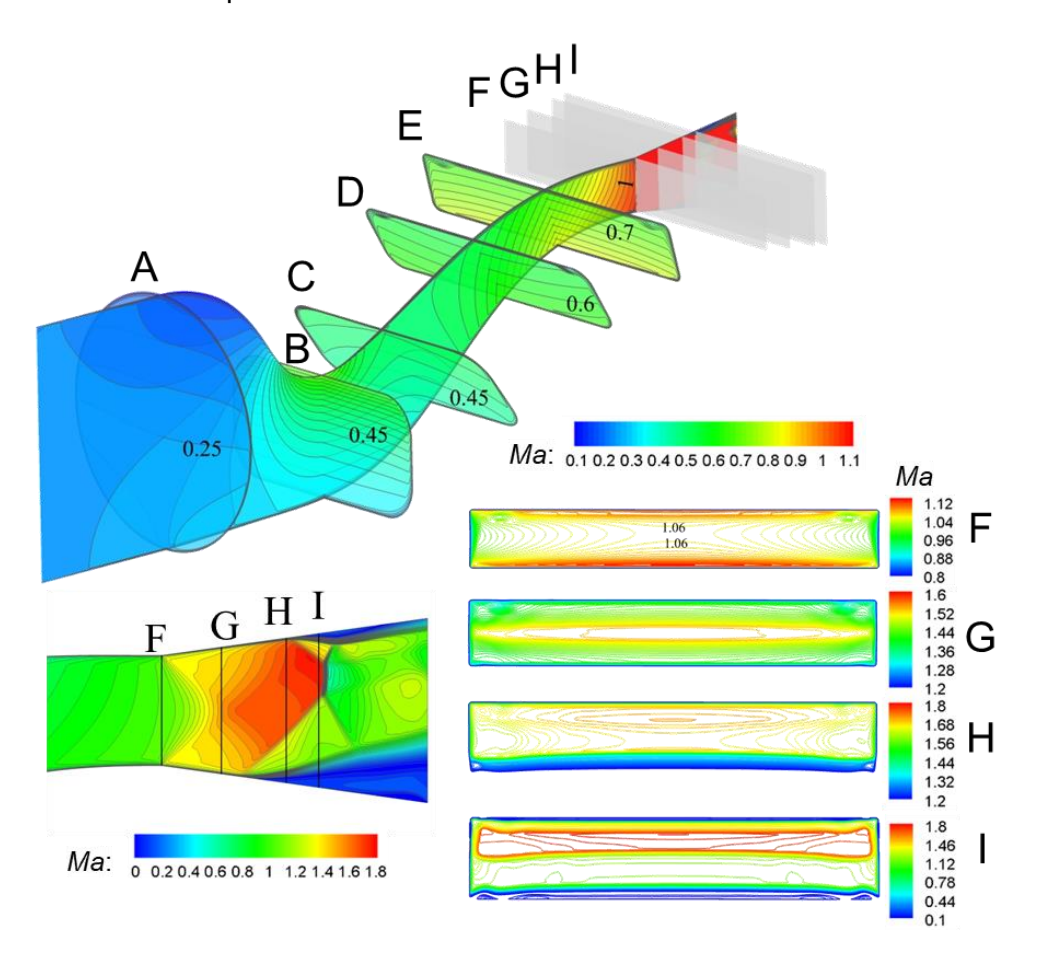


Figure 16 The Mach number on the vertical symmetrical plane and various cross-sections along the path of the nozzle

Figure 17 shows the experimentally measured flux coefficient, thrust vector angle, and axis thrust coefficient at different NPRs. As NPR increases, the flux coefficient increases, the thrust vector angle initially increases and then decreases, and the axial thrust coefficient first decreases and then increases. When NPR is 1.4, flow separation affects the Mach number at the nozzle throat, preventing it from fully reaching Mach 1, resulting in a very low flux coefficient. At pressure ratios between 1.8 and 3.0, the flow coefficient within the nozzle increases slightly due to a slight reduction in overall losses in the serpentine convergent section. The thrust vector angle initially increases because the

flow separation region on the upper side gradually expands, peaking at a NPR of 2.2. As NPR increases to 2.35, the thrust vector decreases slightly because the separation region moves toward the nozzle exit. When NPR increases to 2.45, the flow separation changes from RSS-FSS to FSS-FSS, causing the thrust vector angle to continue decreasing. Subsequently, as NPR further increases, the thrust vector angle continues to decrease, reaching 0° at a NPR of 3, where flow separation becomes symmetric.

The main factors affecting the axial thrust coefficient of the convergent-divergent nozzle include the degree of complete expansion of the airflow, non-axial velocity, and losses within the nozzle. The further the airflow deviates from the fully expanded state, the greater the momentum loss and the axial thrust loss. Losses within the nozzle primarily come from shock wave losses in the divergent section. As NPR increases, the intensity of the shock waves within the nozzle initially increases but then decreases as the shock waves are gradually moved backward, with some wave systems reaching outside the nozzle. At a NPR of 1.4, both shock wave losses and the thrust vector angle are relatively small, resulting in a higher axial thrust coefficient. As NPR increases, the losses due to incomplete expansion of the airflow gradually decrease, while shock wave losses and the thrust vector angle first increase and then decrease. Under the coupled effects of these three factors, the axial thrust coefficient first decreases and then increases, reaching a minimum at a NPR of 2.0.

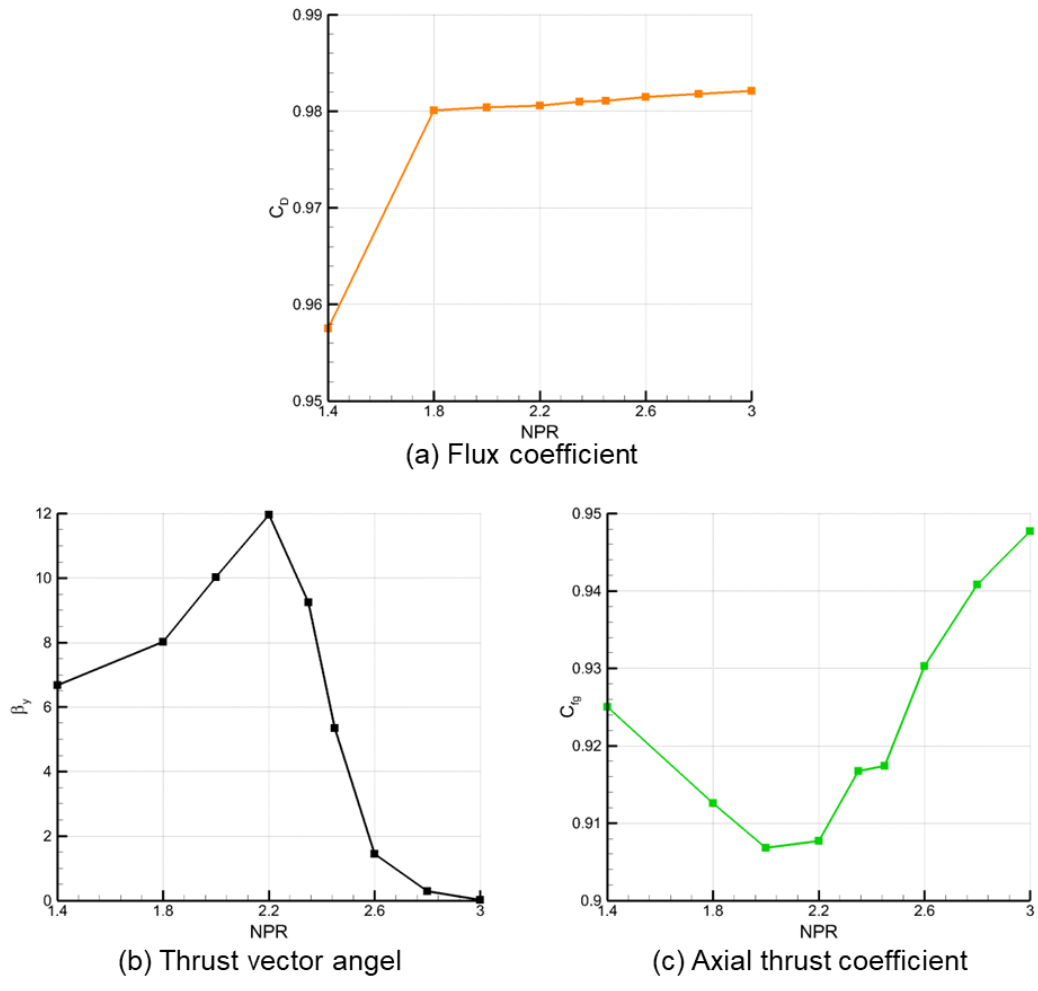


Figure 17 The experimental results of the flux coefficient, thrust vector angle, and thrust coefficient at different NPRs

4. Conclusions

The degree of jet deflection is related to the flow separation structure within the nozzle. As NPR increases, the initial flow separation inside the nozzle is asymmetrical with an upper RSS and a lower FSS, resulting in an upward deflection of the jet. When the upper separation bubble moves out of the

nozzle, it transitions to an asymmetrical FSS-FSS structure, and eventually to a symmetrical FSS-FSS structure. The shock structure inside the nozzle is a double " λ " shock, the shape of which is closely related to the flow separation structure and leads to the formation of a stratified flow in the exit jet. The separation position is influenced by the NPR and flow separation structure. The separation position on the lower wall of the nozzle continuously moves backward as NPR increases, and it is always either ahead of or at the same position as the separation point on the upper wall. The separation point on the upper wall initially moves backward with an increasing NPR. When the upper separation structure changes from RSS to FSS, it moves slightly forward, and then continues to move backward.

The complexity of the flow inside the serpentine convergent section makes the inlet flow of the divergent section show a vertical asymmetry and a lateral non-uniform, which affects the direction of deflection in the divergent section and the variability of the flow separation structure inside different vertical surface, respectively. Influenced by the viscosity of the sidewall surface, there are three-dimensional modes of separation structures inside the nozzle, and a double " λ " shock structure exist in both the vertical plane and the horizontal plane.

When the flow separation affects the Mach number at the throat, the flux coefficient is very low. When the Mach number at the throat reaches 1 overall, the flux coefficient is higher. As NPR increases, the thrust vector angle initially increases then decreases slightly. When the flow separation structure changes from RSS-FSS to FSS-FSS, the thrust vector angle decreases significantly until the flow separation structure becomes symmetrical, at which point the thrust vector angle reduces to 0°. The axial thrust coefficient first decreases and then increases due to the combined effects of the degree of complete expansion of the airflow, non-axial velocity, and losses within the nozzle.

5. Contact Author Email Address

mailto: wangmingxin@mail.nwpu.edu.cn

6. Copyright Statement

The authors confirm that they, and/or their company or organization, hold copyright on all of the original material included in this paper. The authors also confirm that they have obtained permission, from the copyright holder of any third party material included in this paper, to publish it as part of their paper. The authors confirm that they give permission, or have obtained permission from the copyright holder of this paper, for the publication and distribution of this paper as part of the ICAS proceedings or as individual off-prints from the proceedings.

References

- [1] Ball R. E. The fundamentals of aircraft combat survivability: analysis and design: American Institute of Aeronautics and Astronautics, 2003.
- [2] Kopp C. Lockheed-Martin/Boeing F-22 Raptor; Assessing the F-22A Raptor. Air Power Australia, 2007.
- [3] Andersson K. Modeling the impact of surface emissivity on the military utility of attack aircraft. *Aerospace science and technology*, Vol. 65, pp 133-140, 2017.
- [4] Johansson M. and Dalenbring M. Calculation of IR signatures from airborne vehicles. *Modeling and Simulation for Military Applications*, pp 369-380, 2006.
- [5] Johansson M. Propulsion Integration in an UAV. 24th AIAA applied aerodynamics conference, pp 2834, 2006.
- [6] Smith J. and Dalenbring M. Aeroelastic simulation of s-duct dynamics using structure-coupled CFD. *ICAS*, 2006.
- [7] Johansson M. FOT25 2003-20005 propulsion integration final report. Swedish Defence Research Agency (FOI), Stockholm, Sweden, Report No. FOI, 2006.
- [8] Feng N. Development and application of stealth technique. *Int. Technol*, Vol. 119, pp 86-102, 2012.
- [9] Stack C. M. and Gaitonde D. V. Shear layer dynamics in a supersonic rectangular multistream nozzle with an aft-deck. *AIAA Journal*, Vol. 56, No. 11, pp 4348-4360, 2018.
- [10] Hadjadj A. and Onofri M. Nozzle flow separation. Shock Waves, Vol. 19, No. 3, pp 163-169, 2009.
- [11] Nave L. and Coffey G. Sea level side loads in high-area-ratio rocket engines. 9th propulsion conference, pp 1284, 1973.
- [12] Reijasse P., Corbel B. and Soulevant D. Unsteadiness and asymmetry of shock-induced separation in a planar two-dimensional nozzle-a flow description. *30th Fluid Dynamics Conference*, pp 3694, 1999.
- [13] Bourgoing A. and Reijasse P. Experimental analysis of unsteady separated flows in a supersonic planar nozzle. *Shock Waves*, Vol. 14, No. 4, pp 251-258, 2005.
- [14] Papamoschou D. and Zill A. Fundamental investigation of supersonic nozzle flow separation. 42nd AIAA Aerospace

INVESTIGATION ON SEPARATION CHARACTERISTICS OF SERPENTINE C-D NOZZLE

- Sciences Meeting and Exhibit, pp 1111, 2004.
- [15] Papamoschou D., Zill A. and Johnson A. Supersonic flow separation in planar nozzles. *Shock Waves*, Vol. 19, No. 3, pp 171-183, 2009.
- [16] Xiao Q., Tsai H. M. and Papamoschou D. Numerical Investigation of Supersonic Nozzle Flow Separation. *AIAA journal*, Vol. 45, No. 3, pp 532-541, 2007-1-1 2007.
- [17] Xiao Q., Tsai H. M., Papamoschou D., and Johnson A. Experimental and numerical study of jet mixing from a shock-containing nozzle. *Journal of Propulsion and Power*, Vol. 25, No. 3, pp 688-696, 2009.
- [18] Hunter C. A. Experimental, Theoretical, and Computational Investigation of Separated Nozzle Flows. 34th AIAA/ASME/SAE/ASEE Joint Propulsion Conference and Exhibit, 1998.
- [19] Hunter C. A. Experimental Investigation of Separated Nozzle Flows. *Journal of Propulsion and Power*, Vol. 20, No. 3, pp 527-532, 2004.
- [20] Hamed A. and Vogiatzis C. Overexpanded two-dimensional-convergent-divergent nozzle flow simulations, assessment of turbulence models. *Journal of Propulsion and Power*, Vol. 13, No. 3, pp 444-445, 1997.
- [21] Hamed A. and Vogiatzis C. Overexpanded two-dimensional convergent-divergent nozzle performance, effects of three-dimensional flow interactions. *Journal of Propulsion and Power*, Vol. 14, No. 2, pp 234-240, 1998.
- [22] Verma S. B. and Manisankar C. Origin of flow asymmetry in planar nozzles with separation. *Shock Waves*, Vol. 24, No. 2, pp 191-209, 2014.
- [23] Verma S., Chidambaranathan M. and Hadjadj A. Analysis of shock unsteadiness in a supersonic over-expanded planar nozzle. *European Journal of Mechanics B/Fluids*, Vol. 68, pp 55-65, 2018.